Article

Fluorine and Nitrogen Dual-Doped Porous Carbon Nanosheet-Enabled Compact Electrode Structure for High Volumetric Energy Storage

Tianyi Zhu, Siliang Liu, Kening Wan, Chao Zhang,* Yiyu Feng, Wei Feng, and Tianxi Liu*

Cite This: *ACS Appl. Energy Mater.* 2020, 3, 4949−4957

Read Online

ACCESS | Metrics & More | Article Recommendations | Supporting Information

ABSTRACT: The development of electrode materials with high volumetric performance in compact energy storage is extremely appealing, yet challenging. However, the state-of-the-art compact carbon electrodes succumb to an electrode matrix with sluggish ion-transfer kinetics and unsatisfying volumetric performance. Herein, a molten-salt pyrolysis strategy is presented for preparing a fluorine and nitrogen dual-doped porous carbon nanosheet (F/N-CNS). During the molten-salt pyrolysis, nitrogen- and fluorine-rich precursors were converted into a unique two-dimensional carbon nanostructure with in-plane micropores and tailor-made fluorine/ nitrogen dual doping. The as-fabricated thick and compact electrode of the F/N-CNS demonstrates a high packing density of ∼1 g cm^{-3}, fast ion-transfer kinetics, and largely boosted pseudocapacitive characteristics. As a result, the F/N-CNS electrode in a two-electrode configuration exhibits a high volumetric capacitance of 255 F cm^{-3} (1 A g^{-1}), a high volumetric energy density of 18.8 W h L^{-1} in an aqueous electrolyte, and an exceptional cycling stability for 20 000 cycles with almost no capacitance loss. These features demonstrate that the developed F/N-CNS is a promising candidate for high-volumetric-performance electrode materials in next-generation compact energy storage devices.

KEYWORDS: porous carbon nanosheets, fluorine and nitrogen dual doping, molten-salt pyrolysis, ion-transfer kinetics, compact energy storage
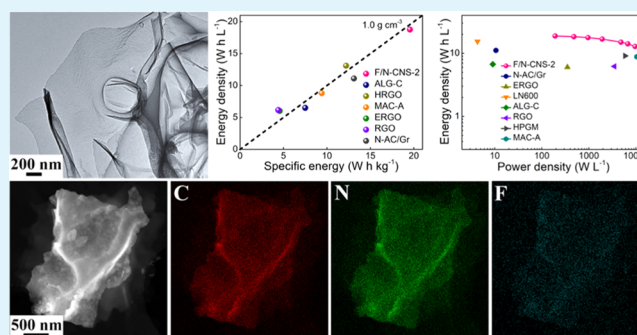
1. INTRODUCTION

Supercapacitors with high performance of fast charging/ discharge property, low maintenance cost, and long cycling life are highly attractive for next-generation energy storage.[1−4] Carbon materials are preferred as promising electrode materials for supercapacitors because they perfectly meet the requirements of high porosity and good electrical conductivity involving the energy storage mechanism of an electrical double-layer capacitor.[5] However, the porous characteristics and low density of carbon materials have become an irreconcilable contradiction limiting the realization of high volumetric performance of carbon electrodes. In the past, the engineering of carbon materials with a hierarchically porous structure enables them with competitively high gravimetric energy density. Consequently, a significant improvement of the porosity of porous carbon materials will unquestionably affect the volumetric performance of the carbon electrode because of the largely reduced packing density of electrodes.[6−8] Therefore, the development of new emerging carbon electrode materials with a high packing density and high volumetric performance is urgently demanded yet challenging.[9−11]

Heteroelement doping is revealed to significantly improve the intrinsic conductivity of carbon electrode materials, as well as boost additional pseudocapacitive performance, thus endowing them with high gravimetric and volumetric capacitances.[12,13] Nitrogen doping (N-doping) is in favor of changing polarity and electron distribution of carbon matrix, thus providing the possibility for achieving efficient ion diffusions.[14] Meanwhile, N-doping also accelerates the migration rate of electrolyte ions by enhancing the wettability at the interface between the electrolyte and the carbon electrode matrix. The increased ion migration rate significantly improves the rate and cycling performance of carbon electrode materials.[15,16] Heteroatom doping, especially like fluorine doping (F-doping), can easily change the electron donor/ acceptor relationship of nearing carbon atoms because of the highest electronegativity of fluorine elements.[17] The highly electronegative fluorine functional groups are effective to refine
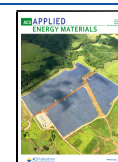
the pore structures/surfaces among the resultant carbon structures.[18] The dual doping of fluorine and nitrogen (F, N dual doping) endowed the resultant carbon electrode materials with increased active sites and largely boosted their pseudocapacitive performance.[19] For heteroatom-doped compact electrode materials, it is evident that the capacitance increases due to the pseudocapacitance introduced by heteroatom doping, but the increase of volumetric capacitances of electrode materials cannot be ignored by reasonably increasing the packing density of electrodes. Therefore, the fabrication of compact carbon electrodes with a high packing density is considered as an important concern for the achievement of high volumetric capacitances of carbon electrode materials.[20] Most of the fluorine doping reactions at present are relatively complex and uncontrollable, generally using toxic and expensive gaseous fluorine-containing reagents. The tightness and safety of equipment for fluorine doping reactions are strictly required. Improper handling of this toxic gas may also cause harm to the environment and personnel. Therefore, the current challenge lies in the development of a green and efficient strategy for preparing fluorine and nitrogen dual-doped carbon materials with controllable doping amount and excellent electrochemical performance.

Herein, a molten-salt pyrolysis strategy is presented for preparing a fluorine and nitrogen dual-doped carbon nanosheet (F/N-CNS) by employing fluorine- and nitrogen-rich organic compounds as the precursor. The molten salt, which is easily molten at a relatively low temperature, is used as a promising "solvent" to provide an ideal reaction medium for the formation of ultrathin carbon architectures with hierarchical porosity. The molten salt not only reduces the release of C-, N-, and F-containing species but also significantly improves the carbonization yield due to a mild and confined pyrolysis process. It is easily removed by simple washing with dilute hydrochloric acid and recycled for subsequent synthesis. Due to the high packing density, fast ion transport, and additional pseudocapacitive behavior of the electrode structure, the F/N-CNS electrode shows a high volumetric energy density, and excellent rate and cycling performance in an aqueous electrolyte.

2. RESULTS AND DISCUSSION

F/N-CNS was pyrolyzed from the powder mixture of nitrogen-rich glucosamine hydrochloride (GLH), fluorine-rich polyvinylidene fluoride (PVDF), and LiCl/KCl eutectic molten salt at 600 °C (Figure 1a). The GLH is a nitrogen-rich organic compound extracted from natural chitin. GLH has been used as a sustainable and low-cost precursor containing carbon and nitrogen species for the synthesis of nitrogen-doped carbon via pyrolysis.[21] Meanwhile, for the carbonization of PVDF, the carbon products typically show a highly porous structure due to the partial escape of the H and F elements. Therefore, the carbon materials prepared by the pyrolysis of PVDF have the characteristics of a uniform nanostructure and a high carbonization yield.[22] F/N-CNS-1, F/N-CNS-2, and F/N-CNS-3 represent the pyrolyzed products prepared by the GLH/PVDF/molten salt weight ratios of 1:0.2:100, 1:1:100, and 1:5:100, respectively. Control samples without PVDF or GLH addition, and direct pyrolysis of neat GLH, PVDF, and GLH/PVDF mixture (1/1, wt/wt) were also prepared and named as F-CNS, N-CNS, N-C, F-C, and F/N-C, respectively, as detailed in the Experimental Section. F/N-CNS-2 exhibits a wrinkled nanosheet morphology with a lateral size of 2−5 μm
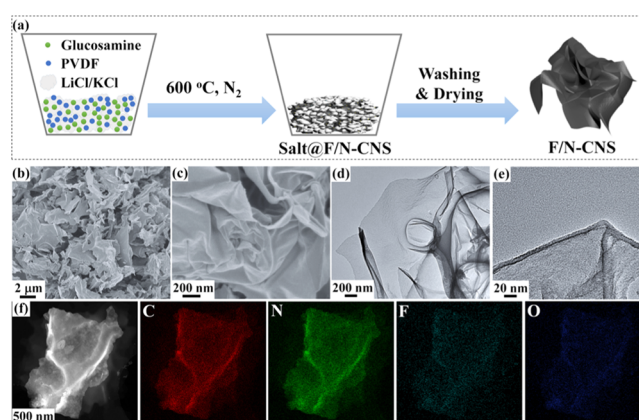

Figure 1. (a) Schematic illustration of the preparation procedure of F/N-CNS. (b, c) Scanning electron microscopy (SEM) and (d, e) transmission electron microscopy (TEM) images of F/N-CNS-2. (f) High-angle annular dark-field scanning transmission electron microscopy (HAADF-STEM) image of F/N-CNS-2 and the corresponding energy dispersive spectroscopy (EDS) elemental mappings.

(Figure 1b,c). No apparent pore structure was found in ultrathin two-dimensional (2D) nanosheets (Figure 1d,e), and uniform elemental distributions of C, N, F, and O are achieved among F/N-CNS-2 (Figures 1f and S1). The variation of the morphological evolution of F/N-CNS by GLH/PVDF feeding ratios is revealed in Figure 2. N-CNS exhibits a nanosheet morphology with the wrinkled surface due to the volume exclusion effect of the molten salt (Figure 2a−c). After adding a small amount of PVDF to the precursor, the morphology of the as-obtained F/N-CNS-1 becomes similar to that of the N-CNS, but the roughness and thickness of carbon nanosheets increase (Figure 2d−f). When PVDF is dominant in the precursor, the F/N-CNS-3 sample shows a thick lamellar morphology (Figure 2g−i). The increased PVDF content in the precursor could increase the contact probability between the primary carbon fragments, which leads to an increase in the thickness of the final carbon nanosheet. GLH is not only used as a nitrogen source but also contributes to PVDF nanosheet structure formation in the presence of molten salt. The morphology of F-CNS can verify this. Without the addition of GLH, F-CNS shows a multilayer morphology with pore sizes below 10 nm (Figure 2j−l). The molten salt during pyrolysis determines the formation of a 2D carbon nanosheet structure. The formation of 2D nanostructures during the molten-salt pyrolysis is probably due to the elimination of primary carbon fragments from molten salt before molten salt crystallization.[23] The control samples of N-C (Figure S2a,b), F/N-C (Figure S2c,d), and F-C (Figure S2e,f) exhibit irregular-shaped bulk carbon structures with rough surfaces due to the absence of molten salts. The direct pyrolysis of precursors such as PVDF and GLH under an inert atmosphere generally leads to a condensation carbonization that proceeds by the elimination of small molecules and often results in a disordered carbonaceous material.

The X-ray photoelectron spectroscopy (XPS) survey spectra indicate the componential information of various elements such as C, N, O, and F among F/N-CNS (Figure S3a). The F 1s XPS spectra of F/N-CNS can be mainly fitted into three peaks (Figure 3a). Three XPS peaks located at 685.9, 687.5, and 689.4 eV are observed in the F 1s XPS spectrum of F/N-
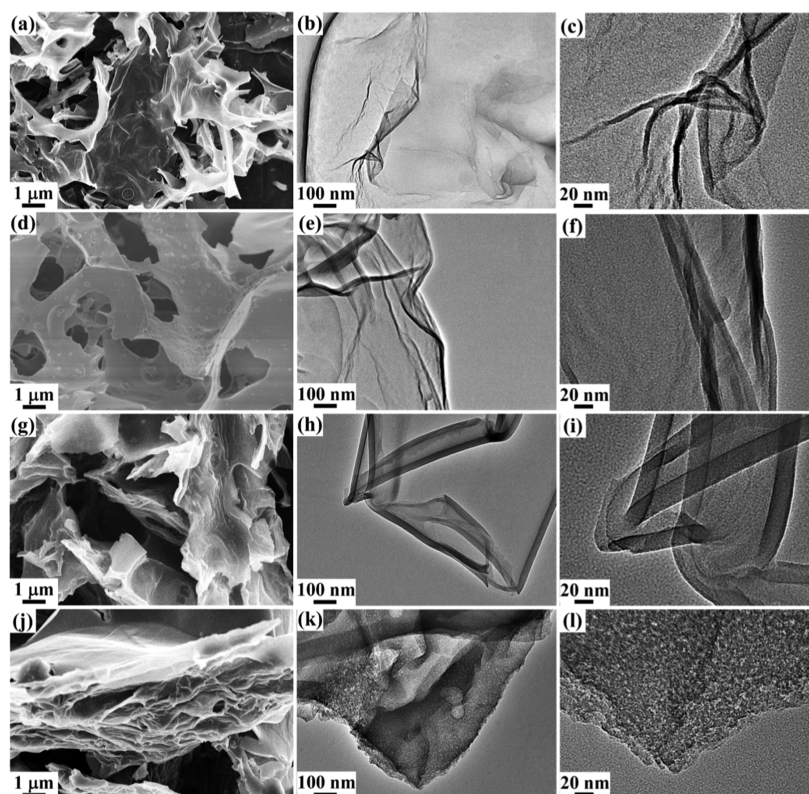
Figure 2. Morphological characterizations of the F/N-CNS sample: SEM and TEM images of (a−c) N-CNS, (d−f) F/N-CNS-1, (g−i) F/N-CNS-3, and (j−l) F-CNS.
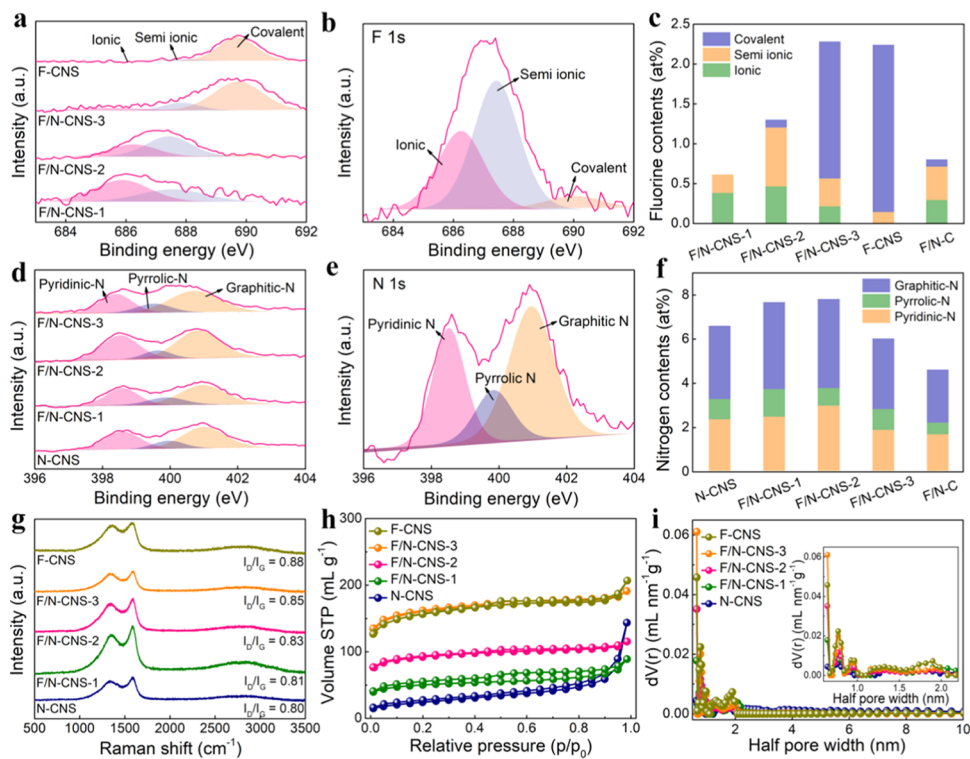

Figure 3. Compositional and structural characterizations of F/N-CNS: (a) High-resolution F 1s XPS spectra of F-CNS, F/N-CNS-1, F/N-CNS-2, and F/N-CNS-3. (b) High-resolution F 1s XPS spectra of F/N-CNS-2. (c) Fluorine contents in terms of covalent, semi-ionic, and ionic C−F in F/N-CNS-1, F/N-CNS-2, F/N-CNS-3, F-CNS, and F/N-C. (d) High-resolution N 1s XPS spectra of N-CNS, F/N-CNS-1, F/N-CNS-2, and F/N-CNS-3. (e) High-resolution N 1s XPS spectra of F/N-CNS-2. (f) Nitrogen contents in terms of graphitic-N, pyrrolic-N, and pyridinic-N in N-CNS, F/N-CNS-1, F/N-CNS-2, F/N-CNS-3, and F/N-C. (g) Raman spectra, (h) nitrogen adsorption/desorption isotherms, and (i) pore size distributions of F-CNS, F/N-CNS-1, F/N-CNS-2, F/N-CNS-3, and N-CNS. The inset of (i shows enlarged microporous regions of i).

Table 1. Comparison of BET Surface Area, Pore Size Distribution, Density, and Carbonization Yield of N-CNS, F/N-CNS-1, F/N-CNS-2, F/N-CNS-3, F-CNS, F/N-C, and F-C Samples

samples	S_{BET} [m² g⁻¹]	pore volume [mL g⁻¹]	micropore volume [mL g⁻¹]	mesopore volume [mL g⁻¹]	tap density [g cm⁻³]	packing density [g cm⁻³]	carbonization yield [wt %]
N-CNS	83	0.07	0.03	0.04	0.07	0.93	34.1
F/N-CNS-1	164	0.11	0.07	0.04	0.05	0.95	35.2
F/N-CNS-2	290	0.15	0.12	0.03	0.09	0.96	36.9
F/N-CNS-3	505	0.26	0.22	0.04	0.22	0.88	39.3
F-CNS	495	0.26	0.21	0.05	0.26	0.85	40.5
F/N-C	428	0.26	0.17	0.09	0.66	0.78	27.9
F-C	784	0.50	0.31	0.19	0.65	0.73	29.1

CNS-2 (Figure 3b), which are ascribed to the ionic, semi-ionic, and covalent C−F bonds, respectively.[24] Among the three typical C−F bonds of F/N-CNS-2, the content of the semi-ionic C−F bond is the highest, about 60% of the total C−F bond content. The semi-ionic C−F bond is formed by the isolated fluorine atoms attached to the surface of carbon nanosheets, which plays a vital role in boosting the pseudocapacitive performance with fast ion and electron transport.[25] The XPS spectra of F/N-CNS-1 and F/N-CNS-3 show that the variety of C−F bonds is strongly related to the composition of the precursor. Figure 3c shows the total content of F elements and the evolution of three C−F bonds in doped carbon. With the increase of the PVDF ratio, the fluorine content in F/N-CNS increased from 0.61 atom % (F/N-CNS-1) to 2.24 atom % (F-CNS), and the ratio of covalent C−F bond also increased. This evolution is mainly due to the increase of the F/C ratio as a result of the increasing proportion of PVDF among the precursors.[26] The XPS results of F/N-CNS-2 and F/N-C show that the proportions of three different C−F bonds in the two samples are almost the same, but the F content in F/N-CNS-2 is significantly higher than that in F/N-C (Figure S3b). The results indicate that the existence of molten salts has a little effect on the evolution of C−F bond species, but can significantly improve the F-doping efficiency. Therefore, the molten salt can provide a confined pyrolysis environment by limiting the release of highly active gas doping agents. The N 1s XPS spectra of N-CNS, F/N-CNS, and F/N-C are deconvoluted to three peaks (Figures 3d,e and S3c), which are assigned to the pyridinic-N (398.4 eV), pyrrolic-N (399.8 eV), and graphitic-N (401.1 eV),[27] respectively. F/N-CNS and N-CNS show similar types of N-doping in terms of graphitic-N, pyridinic-N, and pyrrolic-N due to the use of the same nitrogen sources from the GLH (Figure 3f). The nitrogen content of F/N-C (4.6 atom %) is lower than that of F/N-CNS-2 (7.8 atom %), indicating that the molten salt is in favor of confining the release of gaseous doping agents for the formation of C−N bonds during the pyrolysis. The C 1s XPS spectrum of F/N-CNS-2 can be deconvoluted into a series of peaks (Figure S3d). The XPS peaks at 284.3, 286.3, and 289.2 eV correspond to C−N, CO, and C(O)O bonds, while the XPS peaks at 288.8, 290.3, and 291.8 eV indicate the existence of the semi-ionic C−F bond and two different covalent C−F bond configurations, respectively.[28]

The structural characteristics of the X-ray diffraction (XRD) measurements and the Raman spectra of F/N-CNS, N-CNS, and F-CNS are shown in Figures 3g and S4. The observed diffraction patterns at 25 and 41.6° suggest the formation of the graphitic carbon structure from organic precursors.[29] The Raman peaks of the D and G bands are observed at 1335 and 1585 cm⁻¹, respectively.[30] Moreover, their intensity ratio (I_D/I_G) is usually applied to estimate the defects in the graphitic carbon structure. The intensity ratio I_D/I_G gradually rises from 0.80 (N-CNS) to 0.88 (F-CNS) with the increased PVDF content in precursors, indicating that the in-plane sp² domains of the carbon nanosheets decrease and more defects have been introduced upon the F-doping.

Nitrogen adsorption−desorption measurements were used to evaluate the pore structures of the resultant F/N-CNS (Figures 3h and S5a), and the pore structure data including the specific surface area and pore volume of N-CNS, F/N-CNS, F-CNS, F/N-C, and F-C are summarized in Table 1. The F/N-CNS samples show an obvious hysteresis of the desorption curve in the range of relative pressure from 0.4 to 1.0, indicating that there exists the type IV adsorption behavior with an obvious mesopore structure in the pore structure.[31] Also, the adsorption isotherm is slightly upturned at a relative pressure close to 1.0, revealing that macropores have been introduced. The nitrogen adsorption−desorption isotherms of F/N-CNS show that the as-prepared carbon materials can obtain larger specific surface areas with the increase of the proportion of PVDF in the precursor. The pore volume of N-CNS increases compared to that of F/N-CNS, indicating that a higher proportion of macropore structure is achieved within N-CNS. However, no macropore structure is obtained in the F/N-CNS samples. The presence of PVDF not only effectively increases the specific surface area of the resultant carbon but also refines the pore structure with more micro- and mesopores. The pore size distributions of N-CNS, F/N-CNS, and F-CNS are plotted in Figure 3i, indicating that well-defined micropores of 0.5−2.0 nm exist in F/N-CNS. It is worth to be noted that the pore volume of these samples is lower than that of the carbon samples prepared without the addition of molten salt (Figure S5b). That is, the presence of molten salt benefits the macroscopic rearrangement of the sp²-bond carbon framework and the formation of the densely stacked carbon. The existence of macropores among the carbon samples contributes little to the specific surface area, although it can improve the ion mobility to some extent. Moreover, the presence of macropores will decrease the packing density of carbon electrode materials, thus reducing their volumetric capacitances. F/N-CNS shows a 2D nano-sheet morphology with a wrinkled structure, which shows a fluffy structure and a low tap density. However, its 2D nanosheet features facilitate a high-packing-density electrode fabrication by a simple mechanical compression.[9,32] Table 1
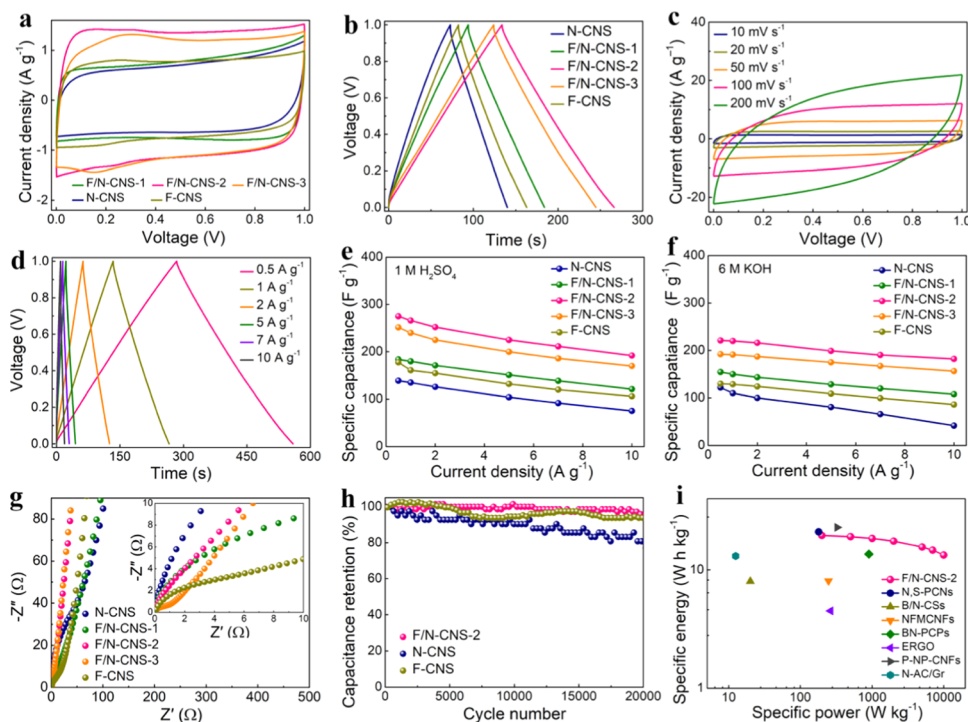
Figure 4. Electrochemical characterizations of F/N-CNS: (a) CV curves of F-CNS, F/N-CNS-1, F/N-CNS-2, F/N-CNS-3, and N-CNS at 10 mV s^{-1} in 1 M H$_2$SO$_4$. (b) Galvanostatic charge/discharge (GCD) curves of F-CNS, F/N-CNS-1, F/N-CNS-2, F/N-CNS-3, and N-CNS at 1 A g^{-1} in 1 M H$_2$SO$_4$. (c) CV curves of F/N-CNS-2 at various scan rates in 1 M H$_2$SO$_4$. (d) GCD curves of F/N-CNS-2 at different current densities in 1 M H$_2$SO$_4$. Specific capacitances of F-CNS, F/N-CNS-1, F/N-CNS-2, F/N-CNS-3, and N-CNS at various current densities in (e) 1 M H$_2$SO$_4$ and (f) 6 M KOH. (g) Nyquist plots of F-CNS, F/N-CNS-1, F/N-CNS-2, F/N-CNS-3, and N-CNS in the frequency range of 100 kHz to 0.01 Hz. The inset of (g shows enlarged high-frequency regions of g). (h) Cycling performance of F-CNS, F/N-CNS-2 and N-CNS for 20 000 cycles in 1 M H$_2$SO$_4$. (i) Ragone plots of the supercapacitor with the F/N-CNS-2 electrode compared to other doped carbon electrodes.

indicates that the packing density of N-CNS, F-CNS-1, and F/N-CNS-2 is significantly higher than that of other samples because the wrinkled nanosheets are easy to deform and assemble into densely stacked carbon structures under compression. The packing density of F/N-CNS-2 is about 0.96 g cm^{-3}, which is close to an ideal packing density of balanced gravimetric and volumetric capacitances.

Molten salt can increase the doping content of heteroatoms by limiting the release of highly active gas doping agents. Interestingly, the carbonization yield of the products is also improved (quantitatively calculated in Table 1), as the molten salt provides a mild and confined environment to prevent the release of gaseous carbon sources during the pyrolysis. For example, F/N-CNS-2 and F/N-C have a similar ratio of GLH and PVDF in the precursor; however, the molten-salt pyrolysis of F/N-CNS-2 exhibits a higher carbonization yield (36.9%) than F/N-C (27.9%). The structural features of high surface area, well-balanced micro/mesoporosity, and 2D nanosheet morphology of F/N-CNS-2 are beneficial for its application as electrode materials with a high packing density, achieving excellent volumetric capacitance for supercapacitors.

Figure 4a shows the cyclic voltammetry (CV) curves of N-CNS, F/N-CNS, and F-CNS electrodes at a scan rate of 10 mV s^{-1} in 1 M H$_2$SO$_4$. The approximate rectangular CV curve shows that the electrode has a fast response behavior of double-layer capacitance with an ideal capacitive behavior. Benefited from the hierarchical pore structure of the nanosheets that realizes a highly efficient ion transport, the F/N-CNS electrodes exhibit a larger CV surrounding area than the N-CNS and F-CNS electrodes in the electrolytes of 1 M

H$_2$SO$_4$ and 6 M KOH (Figures 4a and S6a), respectively. Moreover, the F/N-CNS electrodes demonstrate extra redox pairs compared to the N-CNS and F-CNS electrodes, as the pseudocapacitive behaviors are attributed to additional electrochemically active sites by the F, N dual doping. It is worth noting that the redox peak of the CV curve of the F/N-CNS electrode in the acid electrolyte is more obvious than that in the alkaline electrolyte, which is due to the different electrochemical activities caused by the basic characteristics of F/N dual doping in these carbon samples.[33] The CV curve of the F/N-CNS-2 electrode shows the largest rectangular area compared to the F/N-CNS-1 and F/N-CNS-3 electrodes at the same scanning speed, corresponding to its optimized semi-ionic C−F contents, high surface area, and well-balanced micro/mesopore distributions.

The F/N-CNS-2 electrode also shows the excellent electrochemical properties by the galvanostatic charge/discharge (GCD) characterization (Figures 4b and S6b). Considering the ionic mobility of the acidic electrolyte is slightly higher than that of the basic electrolyte, the specific capacitances of the F/N-CNS electrodes in the acidic electrolyte are larger than that in the basic electrolyte. When the F/N-CNS-2 electrode is scanned in the voltage range of 0−1 V at a scanning rate of 10−200 mV s^{-1}, the CV curve remains approximately rectangular (Figures 4c and S6c), indicating its excellent rate performance. In addition, the GCD curve of the F/N-CNS-2 electrode at different current densities is nearly linear, and the Coulombic efficiency can reach 90% (Figures 4d and S6d), which is due to the high conductivity and rapid ion transport of the electrode matrix

Table 2. Summary of the Electrochemical Parameters of F/N-CNS-2 with Heteroelement-Doped Carbon Materials in the Literature

electrode materials	specific capacitance (current density)	device configuration	electrolyte [mol L^{-1}]	refs
N, S-PCNs	298 F g^{-1} (0.5 A g^{-1})	three-electrode	Na$_2$SO$_4$ (1)	36
B/N-CS	223 F g^{-1} (0.1 A g^{-1})	three-electrode	KOH (6)	37
2D CoSNC	360.1 F g^{-1} (1.5 A g^{-1})	three-electrode	KOH (2)	51
NFMCNFs	252.6 F g^{-1} (0.5 A g^{-1})	three-electrode	H$_2$SO$_4$ (1)	38
a-HHPC	214 F g^{-1} (0.2 A g^{-1})	two-electrode	KOH (6)	52
FNC	168 F g^{-1} (0.5 A g^{-1})	two-electrode	TEA BF$_4$ in PC (1)	53
BN-PCPs	360 F g^{-1} (2 A g^{-1})	three-electrode	H$_2$SO$_4$ (1)	39
CNG	98 F cm^{-3} (1 A g^{-1})	two-electrode	EMImBF$_4$	54
ERGO	176.5 F cm^{-3} (1 A g^{-1})	two-electrode	KOH (6)	40
RGO-HD	255 F cm^{-3} (2 A cm^{-3})	two-electrode	KOH (6)	44
N-doped graphene	300 F cm^{-3} (0.6 A cm^{-3})	three-electrode	KOH (2)	45
NP-OMC	210 F g^{-1} (1 A g^{-1})	three-electrode	KOH (6)	55
P-NP-CNFs	280 F g^{-1} (1 A g^{-1})	three-electrode	KOH (6)	41
CS-650+850	156.9 F g^{-1} (10 A g^{-1})	three-electrode	KOH (6)	56
HRGO	216 F cm^{-3} (1 A cm^{-3})	three-electrode	KOH (6)	57
Th-SNG	284 F g^{-1} (10 mV s^{-1})	three-electrode	KOH (1)	58
N-AC/Gr	257.7 F cm^{-3} (0.05 A g^{-1})	two-electrode	KOH (6)	42
CM-N	200 F cm^{-3} (1 A g^{-1})	three-electrode	H$_2$SO$_4$ (1)	19
F/N-CNS-2	266 F g^{-1}, 255 F cm^{-3} (1 A g^{-1})	two-electrode	H$_2$SO$_4$ (1)	this work

structure. The specific capacitance of the F/N-CNS-2 electrode is larger than 192 F g^{-1} at a high current density of 10 A g^{-1} in the 1 M H$_2$SO$_4$ electrolyte. When the current density increases from 0.5 to 10 A g^{-1}, the capacitance retention of the F/N-CNS-2 electrode is 70 and 82% in the H$_2$SO$_4$ and KOH electrolytes, respectively. It is nearly doubled than the capacitance retention of the N-CNS and F-CNS electrodes, whose specific capacitances decreased about 45 and 40% (Figure 4e,f), respectively. The specific capacitance of the F/N-CNS-2 electrode (192 F g^{-1}) outperforms those of the N-CNS (75 F g^{-1}) and F-CNS (106 F g^{-1}) electrodes, when the current density is 10 A g^{-1}. The excellent capacitance retention performance is promising for the applications where high-rate charge/discharge processes are required.

Figure 4g shows the electrochemical impedance spectroscopy (EIS) of the N-CNS, F/N-CNS, and F-CNS electrodes in the Nyquist diagrams. Because of the slanted lines related to mass transfer in the low-frequency region of these EIS diagrams, these samples exhibit a typical capacitive behavior. The slopes of the F/N-CNS electrodes are steeper than those of the N-CNS and F-CNS electrodes, showing their low ion-diffusion resistances.[34] In the high-frequency region, there are no apparent semicircles in the F/N-CNS electrodes, indicating the low charge transfer resistance between the electrodes and electrolytes due to the sufficient sites on 2D carbon structures.[35] The electrical conductivities of F/N-CNS are measured by four-probe measurements, which are summarized in Table S1. Owing to the unique 2D graphitic structure with a well-balanced porosity, F/N-CNS exhibits superior electrical conductivities from 1.51 to 2.86 S m^{-1} compared to that of F/N-C (1.28 S m^{-1}).

The cycling stability of the N-CNS, F/N-CNS-2, and F-CNS electrodes was evaluated by repeating the GCD tests at the current density of 10 A g^{-1} in the 1 M H$_2$SO$_4$ electrolyte (Figure 4h). Compared to the capacitance retention of N-CNS (87%) and F-CNS (98%), the F/N-CNS-2 electrode shows an extraordinarily long cycling life with almost no capacitance loss after 20 000 charge/discharge cycles. The excellent cycling performance of the F/N-CNS-2 electrode is attributed to the

improved structural stability (Figure S7a,b). The fluorine atoms stabilize the graphitic carbon structure at the edge of carbon lattices, which is able to resist corrosion and shrinkage during repeated charge/discharge processes. Figure 4i presents the Ragone plots of supercapacitors with the F/N-CNS-2 electrodes and other doped carbon electrode materials in the literature. The specific energy of the supercapacitor with the F/N-CNS-2 electrodes reaches up to 17.5 W h kg^{-1}. When the specific powder increases from 2 to 10 kW kg^{-1}, the specific energy of the supercapacitor with the F/N-CNS-2 electrodes only keeps 76.6% with a small drop to 13.4 W h kg^{-1}. The specific energy of the F/N-CNS-2 electrode is superior to that of other doped carbon electrode materials in the literature (Table 2).

Considering the practical applications of carbon electrode materials, the volumetric capacitance of the electrode is an essential parameter of supercapacitors. F/N-CNS-2 with unique structural features of 2D nanosheet with in-plane pores facilitates the fabrication of a compact electrode with a high capacitive behavior. The packing density of the F/N-CNS-2 electrode can be easily improved by mechanical compression.[32] As the packing density increases to 0.96 g cm^{-3}, the volumetric capacitance of the F/N-CNS-2 electrode almost doubles (Figures 5a and S8). The volumetric capacitance of the F/N-CNS-2 electrode can reach 255 F cm^{-3} at a current density of 1 A g^{-1}, much higher than that of the uncompressed F/N-CNS-2 electrode (113 F cm^{-3}) and most of the reported carbon electrodes (Figure 5b).[40,42−45] The ideal packing density of F/N-CNS-2 makes it have excellent gravimetric and volumetric capacitances. F/N-CNS-2 has supreme and comparable performance to other carbon materials with a high packing density (Figure 5c).[40,42,44−47] The F/N-CNS-2 electrode-assembled supercapacitor exhibits a high volumetric energy density of 18.8 W h L^{-1} at a power density of 192 W L^{-1} in the acidic aqueous electrolyte, which is higher than that of most carbon electrode-based super-capacitors reported (Figure 5d).[40,42,44,46−49]

The F/N-CNS electrode has a high specific capacity and good cycle stability, and explanations are as follows. First, the
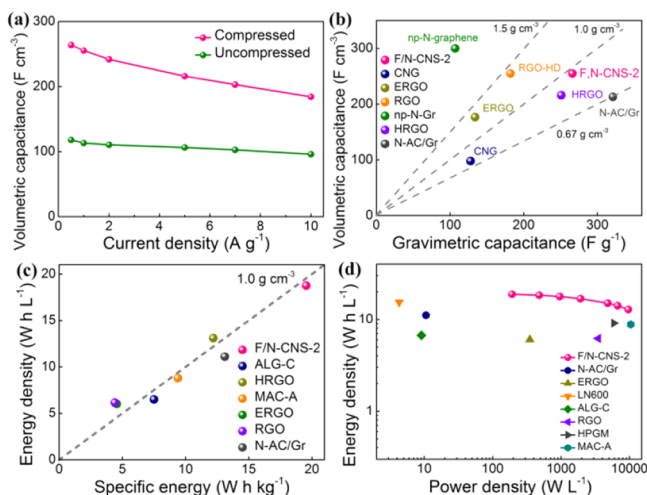
Figure 5. Density−capacitance relationship and device performance. (a) Volumetric capacitances of the F/N-CNS-2 electrode before and after compression. (b) Comparison of volumetric and gravimetric capacitances of F/N-CNS-2 with other doped carbon electrodes in the literature at a high packing density. (c) Comparison of energy density and specific energy of supercapacitors using F/N-CNS-2 and other doped carbon electrodes in the literature. (d) Ragone plots of supercapacitors using F/N-CNS-2 and other doped carbon electrodes in the literature.

molten salt synthesis provides a unique confined pyrolysis environment and synthesis platform for a large-scale preparation of F/N-CNS electrode materials with a high carbonization yield.[23] Second, a high-level F, N dual doping within the F/N-CNS-2 electrode not only effectively improves the wettability of the electrode with electrolytic ions by minimizing the interfacial resistances but also increases the number of redox-active sites for high pseudocapacitances due to enlarged interlayer distances and increased structural defects of F/N-CNS.[50] Third, the high surface area, well-balanced micro/mesoporosity, and 2D nanosheet morphology boost the high volumetric capacitive performance of the F/N-CNS electrodes with a high packing density.

3. CONCLUSIONS

In summary, a molten-salt pyrolysis strategy is presented for preparing F/N-CNS-2 with tunable F and N dual doping. The as-obtained F/N-CNS-2 not only performs fast ion transport due to the unique in-plane pores within the graphitic carbon but also provides an additional pseudocapacitive behavior due to the active sites by the F, N dual doping. The packing density of the F/N-CNS-2 electrode approaches 1 g cm^{-3} after simple compression, which makes it a new-type carbon electrode material with high gravimetric and volumetric energy densities. The F/N-CNS-2 two-electrode supercapacitor device has a high energy density of 18.8 W h L^{-1} at the volumetric power density of 192 W L^{-1}. After 20 000 charge−discharge cycles in acid and alkaline electrolytes, the F/N-CNS-2 electrode has a nearly 100% capacity retention. Therefore, this mild and confined molten-salt pyrolysis strategy provides a green and large-scale approach to prepare 2D dual-doped carbon materials with high carbonization yields and high-level heteroelement doping for compact capacitive energy storage.

4. EXPERIMENTAL SECTION

4.1. Synthesis of F/N-CNS, N-C, F-C, and F/N-C. A powder mixture of GLH (0.10 g) and PVDF was ball-milled with mixed salts (10 g, LiCl/KCl, 45/55, wt/wt) for 30 min. The mixture was pyrolyzed at 600 °C for 2 h at a heating rate of 5 °C min^{-1} in a nitrogen flow. After cooling, the product was washed with dilute hydrochloric acid and deionized water several times and dried in vacuum. F/N-CNS-1, F/N-CNS-2, and F/N-CNS-3 represent the pyrolysis products prepared with 0.02, 0.10, and 0.50 g PVDF, respectively. For comparison, F-CNS and N-CNS were synthesized without GLH and PVDF, respectively, with other conditions the same as F/N-CNS-2 used. N-C, F-,C and F/N-C were directly pyrolyzed from GLH, PVDF, and the mixture of GLH (0.10 g) and PVDF (0.10 g) at 600 °C, respectively.

■ ASSOCIATED CONTENT

ⓢ Supporting Information

The Supporting Information is available free of charge at https://pubs.acs.org/doi/10.1021/acsaem.0c00500.

> Materials characterization; electrochemical characterization; EDS elemental spectrum of F/N-CNS-2; SEM images of N-C, F/N-C, and F-C; XPS survey scans of N-CNS, F/N-CNS, F-CNS, and F-C; F 1s, N 1s XPS spectra of F/N-C; C 1s XPS spectrum of F/N-CNS-2; XRD patterns of F-CNS, F/N-CNS, and N-CNS; nitrogen adsorption/desorption isotherms of F/N-C and F-C; pore size distributions of F/N-C and F-C; comparisons of CV and GCD curves of N-CNS, F/N-CNS, F-CNS, and F-C electrodes in 6 M KOH; CV curves of F/N-CNS-2 in 6 M KOH; GCD curves of F/N-CNS-2 in 6 M KOH; photographs showing compressed F/N-CNS-2 electrode before and after cycling; CV curves of F/N-CNS-2 in 1 M H$_2$SO$_4$ before compression; GCD curves of F/N-CNS-2 in 1 M H$_2$SO$_4$ before compression; and comparisons of electrical conductivities of N-CNS, F/N-CNS, F-CNS, N-C, F-C, and F/N-C (PDF)

■ AUTHOR INFORMATION

Corresponding Authors

Chao Zhang − *State Key Laboratory for Modification of Chemical Fibers and Polymer Materials, College of Materials Science and Engineering, Innovation Center for Textile Science and Technology, Donghua University, Shanghai 201620, P. R. China;* ⓞ orcid.org/0000-0003-1255-7183; Email: czhang@dhu.edu.cn

Tianxi Liu − *State Key Laboratory for Modification of Chemical Fibers and Polymer Materials, College of Materials Science and Engineering, Innovation Center for Textile Science and Technology, Donghua University, Shanghai 201620, P. R. China; Key Laboratory of Synthetic and Biological Colloids, Ministry of Education, School of Chemical and Material Engineering, Jiangnan University, Wuxi 214122, P. R. China; Key Laboratory of Materials Processing and Mold, Ministry of Education, Zhengzhou University, Zhengzhou 450002, P. R. China;* ⓞ orcid.org/0000-0002-5592-7386; Email: txliu@fudan.edu.cn

Authors

Tianyi Zhu − *State Key Laboratory for Modification of Chemical Fibers and Polymer Materials, College of Materials Science and Engineering, Innovation Center for Textile Science and Technology, Donghua University, Shanghai 201620, P. R.*

China; Key Laboratory of Synthetic and Biological Colloids, Ministry of Education, School of Chemical and Material Engineering, Jiangnan University, Wuxi 214122, P. R. China

Siliang Liu − State Key Laboratory for Modification of Chemical Fibers and Polymer Materials, College of Materials Science and Engineering, Innovation Center for Textile Science and Technology, Donghua University, Shanghai 201620, P. R. China

Kening Wan − School of Engineering and Materials Science, Queen Mary University of London, London E1 4NS, United Kingdom

Yiyu Feng − School of Materials Science and Engineering, Key Laboratory of Advanced Ceramics and Machining Technology, Tianjin University, Tianjin 300072, P. R. China; orcid.org/0000-0002-1071-1995

Wei Feng − School of Materials Science and Engineering, Key Laboratory of Advanced Ceramics and Machining Technology, Tianjin University, Tianjin 300072, P. R. China; orcid.org/0000-0002-5816-7343

Complete contact information is available at:
https://pubs.acs.org/10.1021/acsaem.0c00500

Notes

■ REFERENCES

(1) Yu, Z.; Tetard, L.; Zhai, L.; Thomas, J. Supercapacitor Electrode Materials: Nanostructures from 0 to 3 Dimensions. *Energy Environ. Sci.* 2015, 8, 702−730.

(2) Zhang, L. L.; Zhao, X. S. Carbon-Based Materials as Supercapacitor Electrodes. *Chem. Soc. Rev.* 2009, 38, 2520−2531.

(3) Zeng, R.; Deng, H.; Xiao, Y.; Huang, J.; Yuan, K.; Chen, Y. Cross-Linked Graphene/Carbon Nanotube Networks with Polydopamine "Glue" for Flexible Supercapacitors. *Compos. Commun.* 2018, 10, 73−80.

(4) Zhang, Q. Z.; Zhang, D.; Miao, Z. C.; Zhang, X. L.; Chou, S. L. Research Progress in Mno2 -Carbon Based Supercapacitor Electrode Materials. *Small* 2018, 14, No. 1702883.

(5) Borenstein, A.; Hanna, O.; Attias, R.; Luski, S.; Brousse, T.; Aurbach, D. Carbon-Based Composite Materials for Supercapacitor Electrodes: A Review. *J. Mater. Chem. A* 2017, 5, 12653−12672.

(6) Huang, Z.; Li, L.; Wang, Y.; Zhang, C.; Liu, T. Polyaniline/Graphene Nanocomposites Towards High-Performance Supercapacitors: A Review. *Compos. Commun.* 2018, 8, 83−91.

(7) Zhang, W.; Xu, C.; Ma, C.; Li, G.; Wang, Y.; Zhang, K.; Li, F.; Liu, C.; Cheng, H. M.; Du, Y.; Tang, N.; Ren, W. Nitrogen-Superdoped 3d Graphene Networks for High-Performance Supercapacitors. *Adv. Mater.* 2017, 29, No. 1701677.

(8) Yan, J.; Wang, Q.; Wei, T.; Jiang, L.; Zhang, M.; Jing, X.; Fan, Z. Template-Assisted Low Temperature Synthesis of Functionalized Graphene for Ultrahigh Volumetric Performance Supercapacitors. *ACS Nano* 2014, 8, 4720−4729.

(9) Wang, Q.; Yan, J.; Fan, Z. Carbon Materials for High Volumetric Performance Supercapacitors: Design, Progress, Challenges and Opportunities. *Energy Environ. Sci.* 2016, 9, 729−762.

(10) Zhou, J.; Yu, J.; Shi, L.; Wang, Z.; Liu, H.; Yang, B.; Li, C.; Zhu, C.; Xu, J. A Conductive and Highly Deformable All-Pseudocapacitive Composite Paper as Supercapacitor Electrode with Improved Areal and Volumetric Capacitance. *Small* 2018, 14, No. 1803786.

(11) Zhang, C.; Li, H.; Huang, A.; Zhang, Q.; Rui, K.; Lin, H.; Sun, G.; Zhu, J.; Peng, H.; Huang, W. Rational Design of a Flexible Cnts@Pdms Film Patterned by Bio-Inspired Templates as a Strain Sensor and Supercapacitor. *Small* 2019, 15, No. 1805493.

(12) Kopeć, M.; Lamson, M.; Yuan, R.; Tang, C.; Kruk, M.; Zhong, M.; Matyjaszewski, K.; Kowalewski, T. Polyacrylonitrile-Derived Nanostructured Carbon Materials. *Prog. Polym. Sci.* 2019, 92, 89−134.

(13) Hu, C.; Dai, L. Doping of Carbon Materials for Metal-Free Electrocatalysis. *Adv. Mater.* 2019, 31, No. 1804672.

(14) Tian, X.; Lu, X. F.; Xia, B. Y.; Lou, X. W. Advanced Electrocatalysts for the Oxygen Reduction Reaction in Energy Conversion Technologies. *Joule* 2020, 4, 45−68.

(15) Liu, T.; Zhang, L.; You, W.; Yu, J. Core-Shell Nitrogen-Doped Carbon Hollow Spheres/Co3O4 Nanosheets as Advanced Electrode for High-Performance Supercapacitor. *Small* 2018, 14, No. 1702407.

(16) Yu, Q.; Lv, J.; Liu, Z.; Xu, M.; Yang, W.; Owusu, K. A.; Mai, L.; Zhao, D.; Zhou, L. Macroscopic Synthesis of Ultrafine N−Doped Carbon Nanofibers for Superior Capacitive Energy Storage. *Sci. Bull.* 2019, 64, 1617−1624.

(17) Karuppannan, M.; Kim, Y.; Sung, Y.-E.; Kwon, O. J. Nitrogen-Rich Hollow Carbon Spheres Decorated with Feco/Fluorine-Rich Carbon for High Performance Symmetric Supercapacitors. *J. Mater. Chem. A* 2018, 6, 7522−7531.

(18) Jung, M.-J.; Jeong, E.; Kim, S.; Lee, S. I.; Yoo, J.-S.; Lee, Y.-S. Fluorination Effect of Activated Carbon Electrodes on the Electrochemical Performance of Electric Double Layer Capacitors. *J. Fluorine Chem.* 2011, 132, 1127−1133.

(19) Zhou, J.; Lian, J.; Hou, L.; Zhang, J.; Gou, H.; Xia, M.; Zhao, Y.; Strobel, T. A.; Tao, L.; Gao, F. Ultrahigh Volumetric Capacitance and Cyclic Stability of Fluorine and Nitrogen Co-Doped Carbon Microspheres. *Nat. Commun.* 2015, 6, No. 8503.

(20) Feng, S.; Liu, Z.; Yu, Q.; Zhuang, Z.; Chen, Q.; Fu, S.; Zhou, L.; Mai, L. Monodisperse Carbon Sphere-Constructed Pomegranate-Like Structures for High-Volumetric-Capacitance Supercapacitors. *ACS Appl. Mater. Interfaces* 2019, 11, 4011−4016.

(21) Shi, J.; Yan, N.; Cui, H.; Liu, Y.; Weng, Y.; Li, D.; Ji, X. Nitrogen Doped Hierarchically Porous Carbon Derived from Glucosamine Hydrochloride for CO2 Adsorption. *J. CO2 Util.* 2017, 21, 444−449.

(22) Son, I.-S.; Oh, Y.; Yi, S.-H.; Im, W. B.; Chun, S.-E. Facile Fabrication of Mesoporous Carbon from Mixed Polymer Precursor of Pvdf and PtFe for High-Power Supercapacitors. *Carbon* 2020, 159, 283−291.

(23) Liu, X.; Giordano, C.; Antonietti, M. A Facile Molten-Salt Route to Graphene Synthesis. *Small* 2014, 10, 193−200.

(24) Fulvio, P. F.; Brown, S. S.; Adcock, J.; Mayes, R. T.; Guo, B.; Sun, X. G.; Mahurin, S. M.; Veith, G. M.; Dai, S. Low-Temperature Fluorination of Soft-Templated Mesoporous Carbons for a High-Power Lithium/Carbon Fluoride Battery. *Chem. Mater.* 2015, 23, 4420−4427.

(25) An, H.; Li, Y.; Gao, Y.; Cao, C.; Han, J.; Feng, Y.; Feng, W. Free-Standing Fluorine and Nitrogen Co-Doped Graphene Paper as a High-Performance Electrode for Flexible Sodium-Ion Batteries. *Carbon* 2017, 116, 338−346.

(26) Wang, Y.; Lee, W. C.; Manga, K. K.; Ang, P. K.; Lu, J.; Liu, Y. P.; Lim, C. T.; Loh, K. P. Fluorinated Graphene for Promoting Neuro-Induction of Stem Cells. *Adv. Mater.* 2012, 24, 4285−4290.

(27) Zong, W.; Lai, F.; He, G.; Feng, J.; Wang, W.; Lian, R.; Miao, Y. E.; Wang, G. C.; Parkin, I. P.; Liu, T. Sulfur-Deficient Bismuth Sulfide/Nitrogen-Doped Carbon Nanofibers as Advanced Free-Standing Electrode for Asymmetric Supercapacitors. *Small* 2018, 14, No. 1801562.

(28) Wang, X.; Dai, Y.; Jie, G.; Huang, J.; Li, B.; Cong, F.; Jin, Y.; Liu, X. High-Yield Production of Highly Fluorinated Graphene by

Direct Heating Fluorination of Graphene-Oxide. *ACS Appl. Mater. Interfaces* **2013**, *5*, 8294−8299.

(29) Liu, Y.; Xiao, Z.; Liu, Y.; Fan, L.-Z. Biowaste-Derived 3d Honeycomb-Like Porous Carbon with Binary-Heteroatom Doping for High-Performance Flexible Solid-State Supercapacitors. *J. Mater. Chem. A* **2018**, *6*, 160−166.

(30) Wang, L.; Wang, Y.; Wu, M.; Wei, Z.; Cui, C.; Mao, M.; Zhang, J.; Han, X.; Liu, Q.; Ma, J. Nitrogen, Fluorine, and Boron Ternary Doped Carbon Fibers as Cathode Electrocatalysts for Zinc-Air Batteries. *Small* **2018**, *14*, No. 1800737.

(31) Kim, T.; Jung, G.; Yoo, S.; Suh, K. S.; Ruoff, R. S. Activated Graphene-Based Carbons as Supercapacitor Electrodes with Macro- and Mesopores. *ACS Nano* **2013**, *7*, 6899.

(32) Murali, S.; Quarles, N.; Zhang, L. L.; Potts, J. R.; Tan, Z. Q.; Lu, Y. L.; Zhu, Y. W.; Ruoff, R. S. Volumetric Capacitance of Compressed Activated Microwave-Expanded Graphite Oxide (a-MEGO) Electrodes. *Nano Energy* **2013**, *2*, 764−768.

(33) Zhao, L.; Fan, L. Z.; Zhou, M. Q.; Guan, H.; Qiao, S.; Antonietti, M.; Titirici, M. M. Nitrogen-Containing Hydrothermal Carbons with Superior Performance in Supercapacitors. *Adv. Mater.* **2010**, *22*, 5202−5206.

(34) Li, J.; Wang, Y.; Zhou, T.; Zhang, H.; Sun, X.; Tang, J.; Zhang, L.; Al-Enizi, A. M.; Yang, Z.; Zheng, G. Nanoparticle Superlattices as Efficient Bifunctional Electrocatalysts for Water Splitting. *J. Am. Chem. Soc.* **2015**, *137*, 14305−14312.

(35) Jiang, L.; Sheng, L.; Long, C.; Fan, Z. Densely Packed Graphene Nanomesh-Carbon Nanotube Hybrid Film for Ultra-High Volumetric Performance Supercapacitors. *Nano Energy* **2015**, *11*, 471−480.

(36) Li, Y.; Wang, G.; Wei, T.; Fan, Z.; Yan, P. Nitrogen and Sulfur Co-Doped Porous Carbon Nanosheets Derived from Willow Catkin for Supercapacitors. *Nano Energy* **2016**, *19*, 165−175.

(37) Ling, Z.; Wang, Z.; Zhang, M.; Yu, C.; Wang, G.; Dong, Y.; Liu, S.; Wang, Y.; Qiu, J. Sustainable Synthesis and Assembly of Biomass-Derived B/N Co-Doped Carbon Nanosheets with Ultrahigh Aspect Ratio for High-Performance Supercapacitors. *Adv. Funct. Mater.* **2016**, *26*, 111−119.

(38) Na, W.; Jun, J.; Park, J. W.; Lee, G.; Jang, J. Highly Porous Carbon Nanofibers Co-Doped with Fluorine and Nitrogen for Outstanding Supercapacitor Performance. *J. Mater. Chem. A* **2017**, *5*, 17379−17387.

(39) Hao, F.; Yao, Y.; Li, Y.; Tian, C.; Zhang, X.; Chen, J. Synthesis of High-Concentration B and N Co-Doped Porous Carbon Polyhedra and Their Supercapacitive Properties. *RSC Adv.* **2015**, *5*, 77527−77533.

(40) Pham, V. H.; Dickerson, J. H. Reduced Graphene Oxide Hydrogels Deposited in Nickel Foam for Supercapacitor Applications: Toward High Volumetric Capacitance. *J. Phys. Chem. C* **2016**, *120*, 5353−5360.

(41) Xu, G.; Ding, B.; Pan, J.; Han, J.; Nie, P.; Zhu, Y.; Sheng, Q.; Dou, H. Porous Nitrogen and Phosphorus Co-Doped Carbon Nanofiber Networks for High Performance Electrical Double Layer Capacitors. *J. Mater. Chem. A* **2015**, *3*, 23268−23273.

(42) Xie, Q.; Bao, R.; Zheng, A.; Zhang, Y.; Wu, S.; Xie, C.; Zhao, P. Sustainable Low-Cost Green Electrodes with High Volumetric Capacitance for Aqueous Symmetric Supercapacitors with High Energy Density. *ACS Sustainable Chem. Eng.* **2016**, *4*, 1422−1430.

(43) Wang, J.; Ding, B.; Xu, Y.; Shen, L.; Dou, H.; Zhang, X. Crumpled Nitrogen-Doped Graphene for Supercapacitors with High Gravimetric and Volumetric Performances. *ACS Appl. Mater. Interfaces* **2015**, *7*, 22284−22291.

(44) Li, Y.; Zhao, D. Preparation of Reduced Graphite Oxide with High Volumetric Capacitance in Supercapacitors. *Chem. Commun.* **2015**, *51*, 5598−5601.

(45) Qiu, H. J.; Chen, L. Y.; Ito, Y.; Kang, J. L.; Guo, X. W.; Liu, P.; Kashani, H.; Hirata, A.; Fujita, T.; Chen, M. W. An Ultrahigh Volumetric Capacitance of Squeezable Three-Dimensional Bicontinuous Nanoporous Graphene. *Nanoscale* **2016**, *8*, 18551−18557.

(46) Raymundo-Piñero, E.; Leroux, F.; Béguin, F. A High-Performance Carbon for Supercapacitors Obtained by Carbonization of a Seaweed Biopolymer. *Adv. Mater.* **2006**, *18*, 1877−1882.

(47) Hu, J.; Wang, H.; Gao, Q.; Guo, H. Porous Carbons Prepared by Using Metal−Organic Framework as the Precursor for Super-capacitors. *Carbon* **2010**, *48*, 3599−3606.

(48) Kim, D.; Kim, Y.; Choi, K.; Grunlan, J. C.; Yu, C. Improved Thermoelectric Behavior of Nanotube-Filled Polymer Composites with Poly(3,4-Ethylenedioxythiophene) Poly(Styrenesulfonate). *ACS Nano* **2010**, *4*, 513−523.

(49) Tao, Y.; Xie, X.; Lv, W.; Tang, D. M.; Kong, D.; Huang, Z.; Nishihara, H.; Ishii, T.; Li, B.; Golberg, D.; Kang, F.; Kyotani, T.; Yang, Q. H. Towards Ultrahigh Volumetric Capacitance: Graphene Derived Highly Dense but Porous Carbons for Supercapacitors. *Sci. Rep.* **2013**, *3*, No. 2975.

(50) Wang, Y.; Wang, K.; Zhang, C.; Zhu, J.; Xu, J.; Liu, T. Solvent-Exchange Strategy toward Aqueous Dispersible MoS2 Nanosheets and Their Nitrogen-Rich Carbon Sphere Nanocomposites for Efficient Lithium/Sodium Ion Storage. *Small* **2019**, *15*, No. 1903816.

(51) Cao, F.; Zhao, M.; Yu, Y.; Chen, B.; Huang, Y.; Yang, J.; Cao, X.; Lu, Q.; Zhang, X.; Zhang, Z.; Tan, C.; Zhang, H. Synthesis of Two-Dimensional Cos1.097/Nitrogen-Doped Carbon Nanocompo-sites Using Metal-Organic Framework Nanosheets as Precursors for Supercapacitor Application. *J. Am. Chem. Soc.* **2016**, *138*, 6924−6927.

(52) You, B.; Kang, F.; Yin, P.; Zhang, Q. Hydrogel-Derived Heteroatom-Doped Porous Carbon Networks for Supercapacitor and Electrocatalytic Oxygen Reduction. *Carbon* **2016**, *103*, 9−15.

(53) Zhou, H.; Peng, Y.; Wu, H. B.; Sun, F.; Yu, H.; Liu, F.; Xu, Q.; Lu, Y. Fluorine-Rich Nanoporous Carbon with Enhanced Surface Affinity in Organic Electrolyte for High-Performance Supercapacitors. *Nano Energy* **2016**, *21*, 80−89.

(54) Wang, J.; Ding, B.; Xu, Y.; Shen, L.; Dou, H.; Zhang, X. Crumpled Nitrogen-Doped Graphene for Supercapacitors with High Gravimetric and Volumetric Performances. *ACS Appl. Mater. Interfaces* **2015**, *7*, 22284−22291.

(55) Panja, T.; Bhattacharjya, D.; Yu, J.-S. Nitrogen and Phosphorus Co-Doped Cubic Ordered Mesoporous Carbon as a Supercapacitor Electrode Material with Extraordinary Cyclic Stability. *J. Mater. Chem. A* **2015**, *3*, 18001−18009.

(56) Hu, J.; Yang, J.; Duan, Y.; Liu, C.; Tang, H.; Lin, L.; Lin, Y.; Chen, H.; Pan, F. The Synergistic Effect Achieved by Combining Different Nitrogen-Doped Carbon Shells for High Performance Capacitance. *Chem. Commun.* **2017**, *53*, 857−860.

(57) Bai, Y.; Yang, X.; He, Y.; Zhang, J.; Kang, L.; Xu, H.; Shi, F.; Lei, Z.; Liu, Z.-H. Formation Process of Holey Graphene and Its Assembled Binder-Free Film Electrode with High Volumetric Capacitance. *Electrochim. Acta* **2016**, *187*, 543−551.

(58) Kotal, M.; Kim, J.; Kim, K. J.; Oh, I. K. Sulfur and Nitrogen Co-Doped Graphene Electrodes for High-Performance Ionic Artificial Muscles. *Adv. Mater.* **2016**, *28*, 1610−1615.